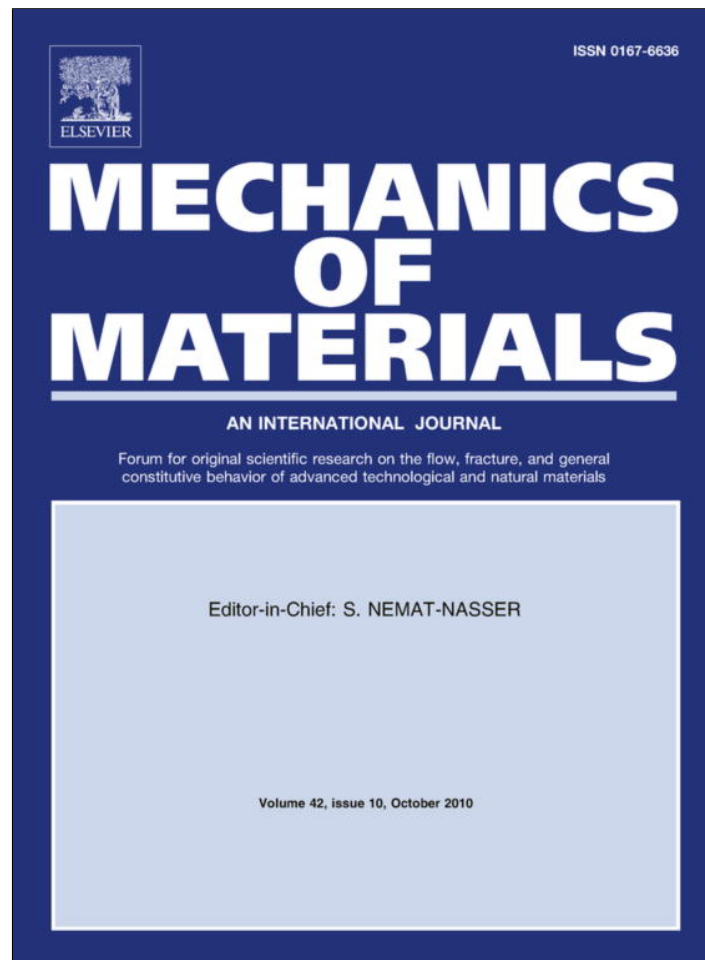


Provided for non-commercial research and education use.
Not for reproduction, distribution or commercial use.



This article appeared in a journal published by Elsevier. The attached copy is furnished to the author for internal non-commercial research and education use, including for instruction at the authors institution and sharing with colleagues.

Other uses, including reproduction and distribution, or selling or licensing copies, or posting to personal, institutional or third party websites are prohibited.

In most cases authors are permitted to post their version of the article (e.g. in Word or Tex form) to their personal website or institutional repository. Authors requiring further information regarding Elsevier's archiving and manuscript policies are encouraged to visit:

<http://www.elsevier.com/copyright>



Contents lists available at ScienceDirect

Mechanics of Materials

journal homepage: www.elsevier.com/locate/mechmat

Combined rate-independent plasticity and creep model for single crystal

Alexander Staroselsky^{a,*}, Brice N. Cassenti^b

^a Pratt & Whitney, 400 Main Street, MS 165-16, East Hartford, CT 06108, USA

^b University of Connecticut, 191 Auditorium Rd. U-3139, Storrs, CT 06269-3139, USA

ARTICLE INFO

Article history:

Received 18 January 2010

Received in revised form 10 June 2010

Keywords:

Creep

Plasticity

Single crystal

Superalloy

Constitutive model

ABSTRACT

There is a need for accurate descriptions of the mechanical state of single crystal blades in gas turbine engines. These components are subject to such extreme temperatures and stresses that life prediction becomes highly inaccurate resulting in components that can only be shown to meet their requirements through experience. To help reduce this inadequacy in current design systems we have developed a thermo-viscoplastic constitutive model for single crystal materials. Our large strain formulation additively decomposes the inelastic strain rate into components along the octahedral and cubic slip planes. Each of these is further additively decomposed into a time dependent creep component and a time independent plastic component. We formulate robust and computationally efficient rate-independent crystal plasticity formulations and combined them with creep flow rules for Ni-based superalloys. The transient variation of each of the inelastic components includes a back stress for kinematic hardening and latent hardening parameters to account for the stress evolution with inelastic strain. Our combined creep and rate-independent formulations for the plastic strains were shown to be accurate when compared to stress–strain and texture evolution measurements. The complete formulation is able to accurately predict both monotonic and cyclic tests at different crystallographic orientations.

© 2010 Elsevier Ltd. All rights reserved.

1. Introduction

In recent years considerable attention has been given to the analysis of the structures and components operating under extreme thermal and mechanical loads. Special interest has arisen in high temperature turbine parts which are subject to long term viscoplastic deformations as well as time independent inelasticity caused by high levels of mechanical stress. This combination of creep and plasticity leads to damage nucleation and growth and a significant reduction of the expected service life. Accurate predictions of material response for combined creep and plastic deformations are complex and greatly compounded during cyclic loading. During service turbine airfoils are subject to strain-controlled cyclic elastic–plastic deformations during airplane maneuvers which are combined with so-called

dwelt times resulting in viscoplastic effects such as creep and/or stress relaxation. Hence, the development of a unified creep–plasticity model capable of predicting cyclic non-isothermal loading conditions is of extreme importance.

The high temperature inelastic behavior of materials has been the subject of considerable research during the last quarter century (see for example, Chaboche, 1986 or Xu and Jiang, 2004). Our constitutive models are based on state variables representing creep, plasticity and damage evolution. The basic physical mechanism of the inelastic deformation analyzed in this paper is dislocation glide or so-called crystallographic slip. We study the Ni-based superalloy PWA 1484 having an $L1_2$ crystallographic structure. Deformation is assumed to occur along the 12 octahedral slip systems $\{111\}\{110\}$ and along the six cube slip systems $\{001\}\{110\}$. Since the cube slip systems resistance is higher than the resistance for the octahedral slip systems, the cube systems activity is limited. However, at

* Corresponding author.

E-mail address: Alexander.Staroselsky@pw.utc.com (A. Staroselsky).

high temperature and for initial crystallographic orientations close to $\langle 111 \rangle$ the γ' particles are sheared by cube systems (Allan, 1995; Stouffer and Dame, 1996). The slip system nomenclature in a single crystal superalloy is shown in Table 1.

Historically, secondary creep effects with associated modeling techniques (Larson–Miller, etc.) were used in engineering calculations. However, during the thermal mechanical loading of high temperature single crystal turbine parts, all creep stages manifest themselves and none of them can be neglected. An adequate creep law is especially important in the case of non-homogeneous thermal loading which results in intensive stress redistribution and relaxation. The inelastic deformation can be decomposed into both creep and plasticity parts. At high temperatures creep is the dominant mode of deformation and because of stress redistribution the applied stress levels remain at moderate levels and do not result in plastic deformation. A description of a plausible creep model is given in Staroselsky and Cassenti (2008). However, after cooling creep deformation simply disappears and inelastic deformation takes place by crystallographic slip which does not vary with temperature as strongly as creep. Our creep experiments show that creep rates follow an Arrhenius type relationship with the value of the activation energy varying in the range from $Q_{(001)} = 6.97E-19$ to $Q_{(111)} = 7.30E-19$ J/atom with some stabilization for the temperatures below 700 °C. Hence, plasticity plays the major role in residual stress generation after cooling during thermal cycling. Thus, a unified model predicting both plasticity and creep effects is needed.

Two approaches can be taken to represent plastic deformation in materials: rate dependent and rate-independent. In rate dependent approaches a constitutive law for the slip rate is assumed, usually in the form of a power law (for example, Asaro, 1983; Asaro and Needleman, 1985; Kalidindi et al., 1992) and slip systems are active even before the resolved shear stress reaches critical values. The rate of inelastic deformation is taken as proportional to the power of the effective resolved shear stress and the corresponding boundary value problem has a unique solution. For large values of the power law exponent the slip

rate will be infinitesimal for small values of the resolved shear stress (RSS), however, if the value of the exponent is small (from 3 to 5), which is the case for creep phenomena, then the slip systems with significant but not the largest values of the RSS are still active and the total shear along these “second order” slip systems could become noticeable. The higher the exponent in the power law the closer this approach gets to the classical plasticity theory. However, the price one has to pay for this is an increase in computational stiffness of the problem and an increase in the computational time. Nevertheless, rate-dependent power law has demonstrated its efficiency and has been widely applied for both monotonic and cyclic problems of plasticity. However, when plastic analysis is combined with creep predictions, the rate dependent nature of the plastic part of the flow rule might cause some problems. A very good example is the inelastic analysis of single crystals of Ni-based superalloys which has a high creep rate at stresses of the order of two thirds of the yield. Let us consider a typical (Nissley et al., 1991; Staroselsky and Cassenti, 2008) rate depended model where the set of calibration parameters are as follows:

$$\dot{\gamma}^\alpha = \dot{\gamma}_0 \left(\frac{\tau^\alpha}{s^\alpha} \right)^m,$$

where $\dot{\gamma}_0 = 0.0001 \text{ s}^{-1}$ and $m = 30$. In a numerical experiment, we applied a constant tensile load at 80% of yield for a time of 100 h using slip resistance, s^α , that accurately fits elastic–plastic stress–strain results. After 100 h the total calculated inelastic deformation was approximately 5%, which is more than a quarter of total observed inelastic deformation to failure. This strain might be eliminated by increasing the exponent to the level of 80 and higher, as shown in Kalidindi and Anand (1994) but this leads to even greater computational difficulties. Therefore, there is a need for the further development of rate-independent crystal plasticity and its combination with creep terms. It is also important to note that rate sensitivity of Ni-based superalloys is small, which in turn leads to high values of the exponent, m .

Hence, a rate-independent formulation should be useful. Some of the earliest time independent formulations were proposed by Krempl et al. (1976), Chaboche (1986) and Walker (1980). Weng (1979, 1980a,b) placed the major emphasis on the formulation of rate-independent plasticity and hardening laws based on dislocation motion concepts and connected them to continuum mechanics theories, such as Hill's anisotropic plasticity model. We used a different approach based on the concept of the yield surface for each potentially active slip system to describe the rate-independent plastic behavior of single crystal materials. This is essentially the application of one dimensional isotropic yield criteria to each crystallographic glide system. Mathematically, it is reduced to the system of linear equations for the slip shear increments. The trial elastic increment is used to select the potentially active slip systems, which in turn is used to construct a set of linear equations. This system should be solved at each incremental step using a numerical method minimizing the errors in some appropriate norm (for example, L_2 norm sense) to

Table 1
Slip systems operative in PWA 1484 at high temperature.

Octahedral		Cube	
α	$(\mathbf{n}^\alpha)[\mathbf{m}^\alpha]$	α	$(\mathbf{n}^\alpha)[\mathbf{m}^\alpha]$
1	$(111)[01\bar{1}]$	13	$(100)[011]$
2	$(111)[\bar{1}01]$	14	$(100)[01\bar{1}]$
3	$(111)[01\bar{1}]$	15	$(010)[101]$
4	$(1\bar{1}\bar{1})[0\bar{1}1]$	16	$(010)[10\bar{1}]$
5	$(1\bar{1}\bar{1})[\bar{1}0\bar{1}]$	17	$(001)[110]$
6	$(1\bar{1}\bar{1})[110]$	18	$(001)[1\bar{1}0]$
7	$(\bar{1}1\bar{1})[011]$		
8	$(\bar{1}1\bar{1})[10\bar{1}]$		
9	$(\bar{1}1\bar{1})[\bar{1}\bar{1}0]$		
10	$(\bar{1}\bar{1}1)[0\bar{1}\bar{1}]$		
11	$(\bar{1}\bar{1}1)[101]$		
12	$(\bar{1}\bar{1}1)[\bar{1}10]$		

give the unique solution for the plastic strain. The idea of the method was originally formulated for the slip systems in FCC crystals under monotonic loading conditions by Anand and Kothari (1996) and generalized for combinations of slip and twin systems by Staroselsky and Anand (1998). However, those models were not able to predict plastic deformation due to cyclic loading and did not account for the effects of kinematic hardening. Also, it is very important to generalize the creep–plasticity calculations for non-isothermal conditions, when deformation resistance parameters change with temperature. In this paper we focus on the development of generic rate-independent crystal plasticity models suitable for cyclic non-isothermal elastic–plastic–viscoplastic analysis.

Summarizing, we decompose the total finite inelastic deformation into plastic and creep parts by incrementally adding current velocity gradients. We formulate a creep power law based on Orowan relation (Orowan, 1940) and examined in detail an approach for describing rate-independent plastic strain behavior in single crystal materials by setting a classical yield condition to each slip system. Our important results are: (1) a combined creep–plasticity formulation for a single crystal, (2) a computationally efficient rate-independent single crystal plasticity model applicable to cyclic plasticity, which does not interfere with a power law creep model when a rate dependent response is also required and (3) a creep flow rule calibrated for Ni-based superalloy and suitable for sigmoidal creep and for tertiary creep prediction. (4) We analyzed non-homogeneous stress and strain distributions such as those that occur in necking.

The plan of the paper is as follows: we start Section 2 with governing equations. The formulation of the creep flow rule is described in Section 3. In the Section 4, we derive a generalization of a rate-independent crystal plasticity model to cyclic deformations. We discuss calibration of the model parameters in the following section. Then, we compare the computational results for different initial crystal orientations and discuss slip system activities including octahedral and cube slip systems in the Section 6. We apply our combined creep and rate-independent plasticity approach to the modeling of simple tension specimen and compare texture evolution, numerical stability, and necking effects with homogeneous numerical solutions and available experimental results. This section also provides results from model predictions for the cyclic deformation of Ni-based superalloys and compares them with coupon testing results. We close the paper with some concluding remarks.

2. Governing equations

The overall plastic response is taken as a sum of responses from small regions of a single crystal playing the role of representative volume elements (RVE). The deformation of a crystal is taken as the sum of contributions from overall elastic distortion and generalized plastic deformation. In this formulation creep will be included in the total inelastic strain rate as will be shown in this sec-

tion. We will denote total inelastic deformation gradient through \mathbf{F}^p for the notation consistency.

The governing variables in the constitutive model are as follows: the Cauchy stress tensor \mathbf{T} and the deformation gradient \mathbf{F} . Each crystal slip system, α , is specified by a unit normal to the slip plane \mathbf{n}_0^α and a unit vector along the slip direction \mathbf{m}_0^α .

The total deformation gradient is multiplicatively decomposed into elastic and inelastic parts as

$$\mathbf{F} = \mathbf{F}^e \mathbf{F}^p \quad \text{and} \quad \det \mathbf{F}^p = 1 \quad (1)$$

The elastic deformation gradient \mathbf{F}^e , ($\det \mathbf{F}^e > 0$) describes elastic distortion and gives rise to the stress \mathbf{T} . The constitutive equation for the second Piola–Kirchhoff stress tensor is taken as a linear relation:¹

$$\mathbf{T}^* = L[\mathbf{E}^e]; \quad \text{where} \quad \mathbf{E}^e(t) = \frac{1}{2}(\mathbf{C}^e(t) - \mathbf{I}); \quad \text{and} \quad \mathbf{C}^e(t) = \mathbf{F}^{eT} \mathbf{F}^e \quad (2)$$

at time, t .

The Cauchy stress tensor is the work conjugate stress corresponding to the Cauchy–Green elastic strain measure and is calculated as follows:

$$\mathbf{T} = \frac{1}{\det(\mathbf{F}^e)} \mathbf{F}^e \mathbf{T}^* \mathbf{F}^{eT} \quad (3)$$

The evolution equation for the viscoplastic deformation gradient is given by the flow rule:

$$\dot{\mathbf{F}}^p = \mathbf{L}^p \mathbf{F}^p \quad \text{where} \quad \mathbf{L}^p = \sum_{\text{slip systems}} \dot{\gamma}^\alpha \mathbf{S}^\alpha \quad \text{and} \quad \mathbf{S}^\alpha = \mathbf{m}^\alpha \otimes \mathbf{n}^\alpha \quad (4)$$

The shear rate along each slip system $\dot{\gamma}^\alpha$ is given in terms of the resolved shear stress (RSS) $\tau = \mathbf{T} \cdot \mathbf{S}^\alpha$, the slip systems resistances and the equilibrium back stress.

Creep is additively included in \mathbf{L}^p as follows: $\mathbf{L}^p = \mathbf{L}^{\text{creep}} + \mathbf{L}^{\text{plasticity}}$. It allows us to combine deformation of creep and rate-independent plastic deformation. At each time (moment) both the plastic and creep deformation increments depend on the cumulative inelastic deformation gradient achieved by this time. If we additionally specify that both creep and plastic deformations take place by slip along specified slip systems, then the total slip increment can be decomposed in the following way: $\Delta\gamma^\alpha = \Delta\gamma_{\text{plastic}}^\alpha + \Delta\gamma_{\text{creep}}^\alpha$.

Evolution of crystallographic texture is explicitly defined by the elastic part of deformation gradient.

$$\begin{aligned} \mathbf{m}_t^\alpha &= \mathbf{F}^e \mathbf{m}_0^\alpha \\ \mathbf{n}_t^\alpha &= \mathbf{F}^{e-T} \mathbf{n}_0^\alpha \end{aligned} \quad (5)$$

We use an incremental formulation where we define all parameters at the end of the time increment $\tau = t + \Delta t$ based on state in the beginning of the increment at time

¹ Generally speaking the elastic relation looks as follows: $\mathbf{T}^* = L[\mathbf{E}^e - \mathbf{A}(\theta - \theta_0)]$, where \mathbf{A} is thermal expansion tensor, θ is current temperature and θ_0 is the reference temperature. All results we report in this paper are valid and derived general formulae and algorithms do not change when we add this thermal strain term. For the sake of simplicity we will use formula (2) in this paper.

t. For the development of the rate-independent plasticity model we need to define a trial step where we assume that the whole increment is elastic, in particular, the plastic deformation gradient is fixed at time t : $\mathbf{F}^{e\ tr}(\tau) = \mathbf{F}(\tau)\mathbf{F}^p(t)^{-1}$. The stress overshoot is compensated for by crystallographic slip. The constitutive relations for the trial step are taken as follows:

$$\begin{aligned} \mathbf{T}^{*tr} &= L[\mathbf{E}^{e\ tr}(\tau)] \\ \mathbf{E}^{e\ tr}(\tau) &= \frac{1}{2}(\mathbf{C}^{e\ tr}(\tau) - \mathbf{I}) \quad \text{and} \\ \mathbf{C}^{e\ tr}(\tau) &= \mathbf{F}^{e\ tr T} \mathbf{F}^{e\ tr} \end{aligned} \quad (6)$$

Substituting (6) into (4) and using expressions (3) one can obtain the relationship between true and trial stress tensors (Kalidindi et al., 1992), which will account for the amount of incremental shear, as:

$$\mathbf{T}^* = \mathbf{T}^{*tr} - \sum_{\alpha} L[\text{sym}(\mathbf{C}^{e\ tr} \mathbf{S}_0^{\alpha})] \Delta \gamma^{\alpha} \quad (7)$$

and the trial resolved shear stress along each slip system is

$$\tau^{e\ tr} = \mathbf{T}^{*tr} \mathbf{S}_0^{\alpha} \quad (8)$$

Expression (4) will then have the incremental flow rule form as follows:

$$\mathbf{F}^p(\tau) = \mathbf{L}^p(\tau) \mathbf{F}^p(t) = \left(1 + \sum_{\alpha} \Delta \gamma^{\alpha} \mathbf{S}_0^{\alpha} \right) \mathbf{F}^p(t) \quad (9)$$

In order to complete governing equations we have to formulate the specific flow rules for creep and plasticity.

3. Creep flow rule

We use Orowan's assumption that the creep strain rate is proportional to the density of the mobile dislocations or in other words, the dimensionless parameter $\frac{\rho_m}{\rho_0}$ where ρ_0 is the initial dislocation density, serves as a measure of the mobile dislocation density, and can be used to predict creep of single crystal. We have used a standard viscoplastic power law creep with a back stress to represent the response of the material or, in other words, the dislocation velocity term in the Orowan relation. The constitutive law for the creep strain rate along α th slip system $\{\dot{\gamma}^c\}^{\alpha}$ is to be written as follows:

$$\{\dot{\gamma}^c\}^{\alpha} = \dot{\gamma}_0 \left(\frac{\rho_m^{\alpha}}{\rho_0} \right) \left| \frac{\tau^{\alpha} - \omega^{\alpha}}{s^{\alpha}} \right|^n \text{sign}(\tau^{\alpha} - \omega^{\alpha}) \exp\left(-\frac{Q}{k\Theta}\right) \quad (10)$$

where $\dot{\gamma}_0$ is a temperature dependent time constant, and s^{α} is the deformation resistance of α th slip system; τ^{α} is the resolved shear stress. The Arrhenius term accounts for the temperature dependence, ω^{α} is the slip system back stress, n is the creep exponent set to be equal to three in this work.

Next, latent hardening evolution has been described by Asaro's (1983) hardening rule $\dot{s}^{\alpha} = h_0 (1 - \frac{s^{\alpha}}{s^*})^p \sum_{\beta} h^{\alpha\beta} |\dot{\gamma}^{\beta}|$, with hardening matrix $h^{\alpha\beta} = \{q + (1 - q)\delta^{\alpha\beta}\}$ for temperature dependent h_0 and s^* , and constant $q = 1.4$.

We model cyclic effects and primary creep effects by defining for each slip system a specific internal equilibrium, or back stress, ω . The back stress has a limiting sat-

uration value $\omega_{\infty} = \frac{c_1}{c_2}$, corresponding to the stabilization of the equilibrium portion of the stress (i.e., the portion of the stress that has not yet contributed to the inelastic strain) and evolves according to the following relationship (Nissley et al., 1991; Voyiadjis and Huang, 1996; Stouffer and Dame, 1996):

$$\dot{\omega}^{\alpha} = c_1 \dot{\gamma}^{\alpha} - c_2 |\dot{\gamma}^{\alpha}| \omega^{\alpha} \quad (11)$$

Eq. (11) requires two additional coefficients c_1 and c_2 that are explicit functions of temperature. It is important to note that hardening terms indirectly account for rafting and microstructure evolution specific for superalloys during the first stage of creep. Thus, material microstructure evolution is accounted by appropriate calibration of hardening state variables. Note that, Eq. (11) is also rate-independent since the derivative of ω^{α} can be written with respect to $\dot{\gamma}^{\alpha}$ making ω^{α} a single variable function of $\dot{\gamma}^{\alpha}$. The effect of voids on the slip rate can be calculated through a correction of the effective stress which is equivalent to a Kachanov-type damage parameter (Kachanov, 1986; Lemaitre, 1996). For the sake of simplicity we will not consider the effects of voids in this paper.

As everywhere in this paper, for the inelastic deformation mechanisms we use the 12 octahedral slip systems $\langle 110 \rangle (111)$. At high temperatures the cube slip systems $\langle 110 \rangle (001)$ may also contribute to maintaining the plastic flow of superalloys. The material model parameters are different for the octahedral and cube slip systems.

Dislocation generation and motion represents a non-recoverable state for the material. These states can be related to the energy for the system through equilibrium statistical mechanics. We postulate that dislocation generation rate is proportional to the rate of entropy production. We consider two types of the dislocations: mobile and pinned. The mobile and the pinned dislocations densities evolve over time. Using concepts from chemical kinetics we have chosen to represent the evolution as two body interactions. We assume that dislocation immobilization takes place when two corresponding dislocation loops interact with each other. Taking into account that $\{\dot{\gamma}^c\}^{\alpha}$ is already a linear function of the mobile dislocation density to represent two body interactions we immediately obtain relations for mobile and pinned dislocations evolution along each slip system:

$$\begin{aligned} \dot{\rho}_m^{\alpha} &= M \left(\frac{\tau^{\alpha} - \omega^{\alpha}}{s^{\alpha}} \right) \dot{\gamma}^{\alpha} \left(\frac{\varepsilon^2 \rho_m^{ss} + \rho_p^{ss} - \rho_p^{\alpha} - \varepsilon^2 \rho_m^{\alpha}}{\rho_0} \right) \\ \dot{\rho}_p^{\alpha} &= \Pi \left(\frac{\tau^{\alpha} - \omega^{\alpha}}{s^{\alpha}} \right) \dot{\gamma}^{\alpha} \left(\frac{\rho_p^{ss} - \rho_p^{\alpha}}{\rho_0} \right) \end{aligned} \quad (12)$$

where M and Π represents specific time constants, different for octahedral and cube slip systems, ρ_m^{ss} is the saturated mobile dislocation density, ρ_p^{ss} is the saturated pinned dislocation density, and ε^2 is a positive constant. Eq. (12) includes the generation of mobile dislocations and also include their conversion to pinned dislocations.

These equations conclude the formulation of the creep part of the model. State variables and material parameters have been calibrated against isothermal creep tests conducted at different crystallographic orientations, at a wide

range of temperatures varying from 700 to 1100 °C, and at different nominal tensile stresses.

4. Generalization of incremental linear system formulation to cyclic plasticity

In the rate-independent (RI) model, the system will be active only if the effective RSS is equal to slip resistance (i.e., the yield stress). Then

$$\dot{\gamma}^\alpha = \begin{cases} 0, & \text{if } |\tau^\alpha - \omega^\alpha| < s^\alpha(\tau) \text{ or } (\tau^\alpha - \omega^\alpha)\dot{\omega}^\alpha < 0, \text{ (unloading)} \\ \geq 0, & \text{if } |\tau^\alpha - \omega^\alpha| = s^\alpha(\tau) \text{ and } (\tau^\alpha - \omega^\alpha)\dot{\omega}^\alpha \geq 0, \text{ (loading)} \end{cases} \quad (13)$$

In this section, we will reduce the problem to a system of the linear equations with respect to shear increments. Substituting relationship (7) into the expression for the trial RSS (8), we immediately obtain:

$$\begin{aligned} \tau^\alpha &= \tau^{\alpha tr} - \sum_{\beta} L(\text{sym}(\mathbf{C}^{e tr} \mathbf{S}_0^\beta)) \mathbf{S}_0^\alpha \Delta \gamma^\beta \\ &= \tau^{\alpha tr} - \sum_{\beta} L(\text{sym}(\mathbf{C}^{e tr} \mathbf{S}_0^\beta)) \mathbf{S}_0^\alpha |\Delta \gamma|^\beta \text{sign}(\tau^{\beta tr} - \omega^\beta) \end{aligned} \quad (14)$$

Following the idea of Anand and Kothari (1996), for the next step we assume that for a small strain increment, changes in the slip directions:

- (i) will be the same for the true and trial increments $\text{sign}(\tau^\alpha - \omega^{\alpha tr}) = \text{sign}(\tau^\alpha - \omega^{\alpha tr})$, and
- (ii) the effect of change in back stress values during one increment does not affect the slip direction: $\text{sign}(\tau^\alpha(\tau) - \omega^\alpha(t))$.

These assumptions are needed to compute the absolute values of the effective resolved shear stress used in the yield criterion $|\tau^\alpha(\tau) - \omega^\alpha(\tau)|$.

The systems for which trial values of effective shear stress are less than the slip resistance in the beginning of increment $s(t)$ are called inactive and are not analyzed during the increment. For the other or so-called “potentially active” slip systems, the absolute value of the effective shear stress can be calculated through the resolved shear stress trial value using

$$|\tau^\alpha - \omega^\alpha| = |\tau^{\alpha tr} - \omega^\alpha(\tau)| - \sum_{\beta} L(\text{sym}(\mathbf{C}^{e tr} \mathbf{S}_0^\beta)) \mathbf{S}_0^\alpha |\Delta \gamma|^\beta \text{sign}(\tau^\beta - \omega^\beta) \text{sign}(\tau^\alpha - \omega^\alpha) \quad (15)$$

Using the incremental formulation for the back stress (11):

$$\omega^\alpha(\tau) = \omega^\alpha(t) + (c_1 \text{sign}(\Delta \gamma^\alpha) - c_2 \omega^\alpha(t)) |\Delta \gamma^\alpha|$$

We immediately obtain the result

$$|\tau^{\alpha tr} - \omega^\alpha(\tau)| = |\tau^{\alpha tr} - \omega^\alpha(t)| - (c_1 - c_2 \omega^\alpha(t)) \text{sign}(\tau^{\alpha tr} - \omega^\alpha(t)) |\Delta \gamma^\alpha| \quad (16)$$

Finally, using the latent hardening evolution equation $s^\alpha(\tau) = s^\alpha(t) + \sum_{\beta} h^{\alpha\beta} |\Delta \gamma^\beta|$ we reduce the problem of finding absolute values of slip increments determination to a solution of the linear system,

$$\mathbf{B} |\Delta \gamma| = \mathbf{b} \quad (17)$$

where $|\Delta \gamma|$ is the vector of absolute values of shears along potentially active slip systems;

$$\begin{aligned} B^{\alpha\beta} &= h^{\alpha\beta} + (c_1 - c_2 \omega^\alpha(t)) \text{sign}(\tau^{\alpha tr} - \omega^\alpha(t)) \\ &\quad + \mathbf{S}_0^\alpha L(\text{sym}(\mathbf{C}^{e tr} \mathbf{S}_0^\beta)) \text{sign}(\tau^{\beta tr} - \omega^\beta) \text{sign}(\tau^{\alpha tr} - \omega^\alpha) \\ b^\alpha &= |\tau^{\alpha tr} - \omega^\alpha(t)| - s^\alpha(t) \end{aligned} \quad (18)$$

This system has a number of variables equal to the number of “potentially active” slip systems, however, not all of the linear equations are always linearly independent. The system might be solved using any appropriate approximation scheme from numerical linear algebra. One of the “proven” and effective algorithms is SVD (Singular Value Decomposition) which gives the least square solution. We do not discuss the advantages and disadvantages of different linear algebra algorithms and use SVD throughout this paper.

5. Calibration of model parameters

Anisotropic elastic properties are defined by three different moduli that change with temperature. Spline fits of the experimental measurements are shown in Fig. 1. The fourth order elasticity tensor has the form specific for orthotropic materials with cubic symmetry:

$$\begin{aligned} C_{iiii} &= C11; \quad (i = 1, 3) \\ C_{ijij} &= C12; \quad (i, j = 1, 3) \\ C_{ijji} &= C44; \quad (i, j = 1, 3) \end{aligned}$$

We consider single crystal Asaro hardening behavior with the parameters h_0 and initial value of slip resistance s_0 for both octahedral and cube systems which are also functions of temperature. We focused on the plasticity and creep analysis for two crystallographic corner orientations $\langle 001 \rangle$ and $\langle 111 \rangle$. The material parameters were found by matching the results with monotonic uniaxial tensile elastic–plastic tests at a number of temperature values and then a spline to interpolate for intermediate temperatures.

We calibrated our creep–plasticity model predictions against isothermal strain-controlled monotonic tensile test results obtained for different temperatures. This calibration provides us initial results for slip resistance s_0 and h_0 that are shown in Fig. 2.

Creep tests were performed under constant load conditions and the test results were converted to true stress and true strain values. Fig. 3 compares predicted and experimentally measured creep curves for a typical test conditions. Similar results were obtained over a wide range of temperatures and applied stresses for both $\langle 001 \rangle$ and $\langle 111 \rangle$ crystallographic orientations (see details in Staroselsky and Cassenti, 2008). Comparing calculated creep strain vs. time curves against test data we calibrated the parameters for kinematic hardening (back stress) and dislocation evolution. Specifically, these creep test results were used to find the constants c_1 and c_2 in the evolution equation for ω , and to obtain a refined estimate for the latent hardening parameters, s_0 and h_0 . The results for

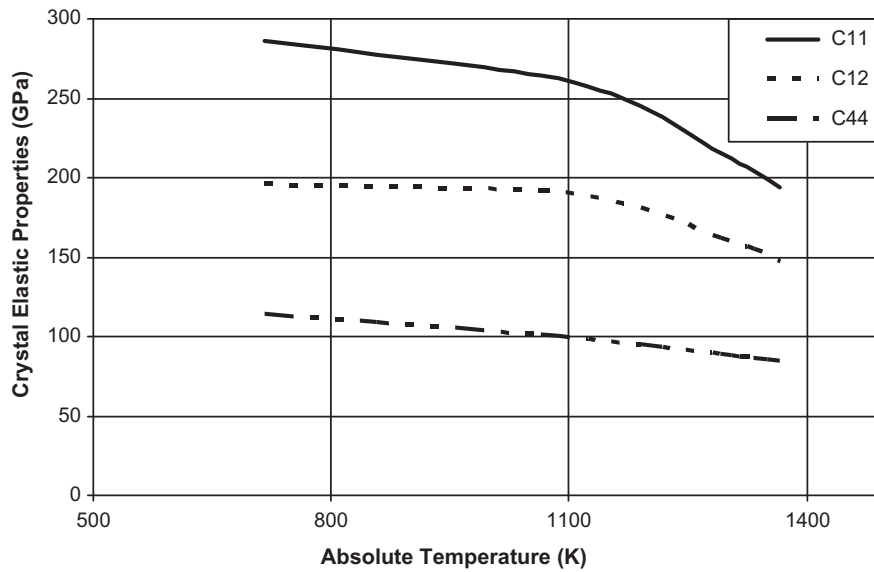


Fig. 1. Variation of elastic properties with temperature.

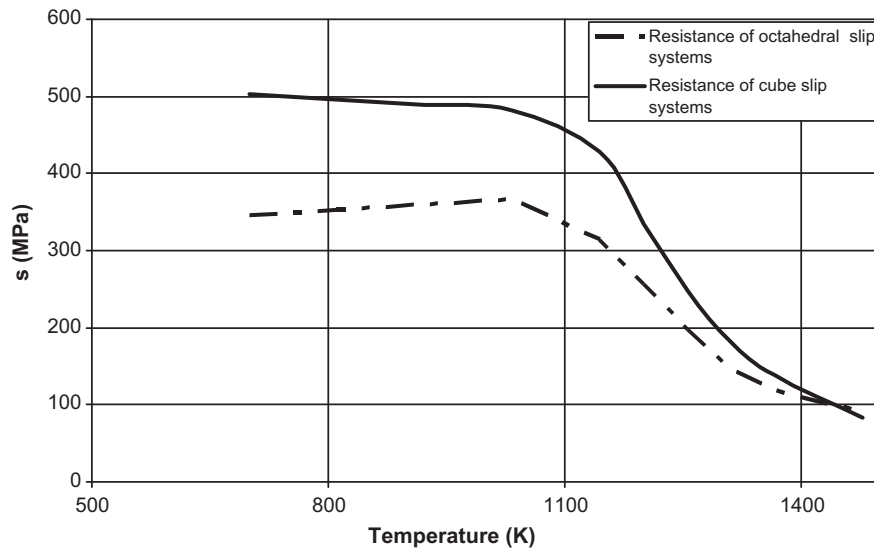


Fig. 2. Variation of initial slip resistances for octahedral and for cube slip systems with temperature.

$\omega_\infty = \frac{c_1}{c_2}$ and the constant c_2 for both octahedral and cube systems are shown in Fig. 4. We chose the mobile dislocation equilibrium density to be 10^5 of the initial density and the pinned dislocation saturation density to be 10^3 of the initial density. Table 2 lists the values of other specific model parameters.

The revised parameters were then checked against the monotonic uniaxial tensile elastic–plastic test results and the parameters were refined. We then repeated the refinement of the parameters for creep and plasticity tests until a satisfactory set of parameters was obtained.

Having obtained the parameters for the octahedral slip system tests along the $\langle 0\ 0\ 1 \rangle$ crystallographic orientation, we then repeated the same procedure to calibrate the cube slip system parameters, and then compared the total model predictions against $\langle 1\ 1\ 1 \rangle$ tests.

As one can see from Fig. 4 the maximum value of the back stress ω_∞ for cube systems is much higher at low

temperatures and drops rapidly with the temperature increase. Combining the drop in the maximum back stress with the rapid decrease of the latent hardening cube slip resistance with temperature shows the increasingly important role of cube systems at high temperature and their very limited effect on inelastic deformation at low temperatures. It is important to note that during the generic elastic–viscoplastic deformation, the model state variables and parameters evolve simultaneously due to creep and plastic deformation.

6. Computational results

6.1. Monotonic loading for various crystallographic orientations

In this section, we compare the predictions obtained by our new rate-independent plasticity model against

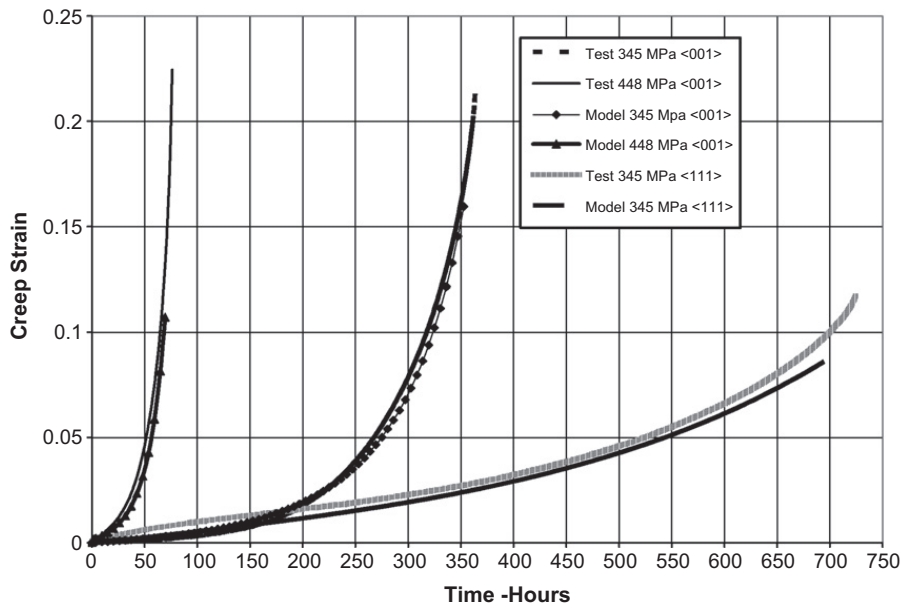


Fig. 3. Prediction vs. experimentally obtained creep curves for PWA 1484 under uniaxial tension along $\langle 001 \rangle$ and $\langle 111 \rangle$ crystallographic directions at 927 °C.

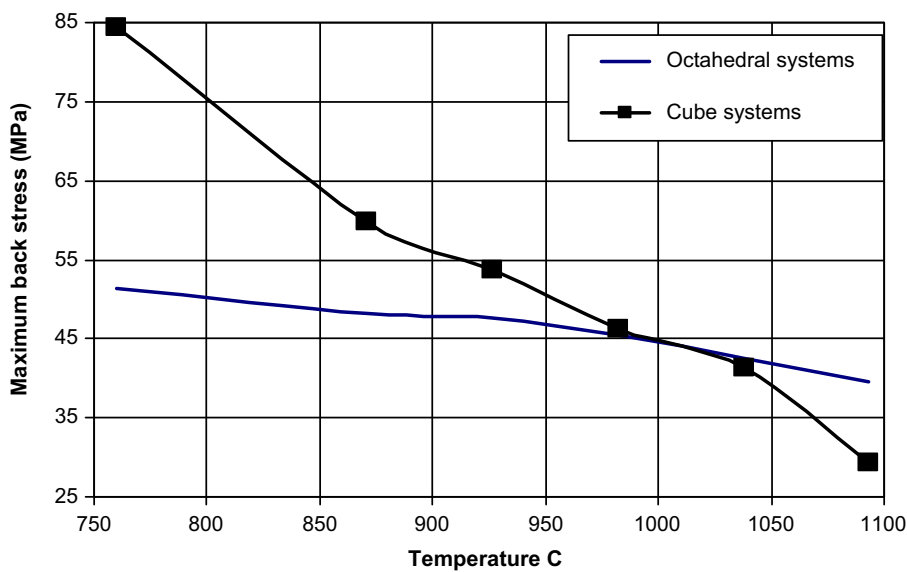


Fig. 4. Variation of back stress ω_{∞} for octahedral and for cube slip systems with temperature.

predictions obtained by a power law, and the solution of the linear system described in section 2, with available experimental data. We discuss single crystal Ni-based superalloy constitutive behavior at relatively high temperatures where the loading applied along one of the corner orientation $\langle 001 \rangle$ or $\langle 111 \rangle$ and along an internal orientation of $\langle 236 \rangle$ and $\langle \bar{1}23 \rangle$.

Using the developed constitutive models we performed simulations of displacement controlled simple tension tests. We used ANSYS 8-node brick elements (element type 185) for both single element simulations and a 3744 element cylinder simulation. Single element simulations satisfy homogeneous uniaxial stress and strain distribution. Analysis shows that two types of boundary conditions pro-

vide the required uniaxial stress–strain distribution. We will call the single element where the upper and lower surfaces remain parallel and orthogonal to the displacement direction element type A. The element with two vertical sides parallel to the loading direction will be called element type B. Both elements and sketches illustrating the deformation of each type are shown in Fig. 5 (from Dieter, 1988).

There is no numerical difference between predictions of single elements for A or B types subject to simple tension with the high symmetry orientations $\langle 001 \rangle$ and $\langle 111 \rangle$ (i.e., corner locations in a stereographic projection) due to highly homogeneous deformation. Moreover, the single element prediction is exactly the same as the numerical predictions obtained from cylinder calculations. Crystal

Table 2
Calibrated model parameters.

θ	871	982	1038	$^{\circ}\text{C}$
<i>Octahedral</i>				
$\dot{\gamma}_0 \exp(-Q/k\theta)$	8.61E-09	1.52E-07	3.22E-07	1/s
h_0	220	124	55	MPa
s^*	824	618	618	MPa
s_0	313	197	145	MPa
$M\rho_0$	0.069	0.067	0.059	
$\Pi\rho_0$	0.05	0.525	0.647	
ε^2	0.55	0.45	0.45	
<i>Cubic</i>				
$\dot{\gamma}_0 \exp(-Q/k\theta)$	1.82E-08	9.87E-08	2.14E-07	1/s
h_0	220	220	220	MPa
s^*	427	247	182	MPa
s_0	824	824	618	MPa
$M\rho_0$	0.07	0.0515	0.05	
$\Pi\rho_0$	0.008	0.225	0.5	
ε^2	0.65	0.4	0.4	

orientation does not change during the numerical tests in both corner orientations. There are eight equally active octahedral systems for $\langle 001 \rangle$ crystallographic orientation tests. The stress–strain curves obtained by methods described above and also experimentally measured for 980 °C are shown in Fig. 6a. There are six equally active octahedral slip systems $(111)[\bar{1}01]$, $(111)[01\bar{1}]$, $(\bar{1}\bar{1}\bar{1})[011]$, $(\bar{1}\bar{1}\bar{1})[10\bar{1}]$, $(\bar{1}\bar{1}\bar{1})[0\bar{1}\bar{1}]$ and $(\bar{1}\bar{1}\bar{1})[\bar{1}10]$ as well as three identically active cube slip systems $(100)[011]$, $(010)[10\bar{1}]$, and $(001)[1\bar{1}0]$ observed during simulations of simple tension along a $\langle 111 \rangle$ crystallographic orientation. The normalized stress–strain curves for this crystallographic orientation at 980 °C are shown in Fig. 6b.

When loaded along a central direction inside the primary stereographic triangle the crystal deforms initially along a single slip system with the highest value of resolved shear stress (i.e., with the highest value of Schmidt factor). Usually such a deformation is very unstable. We

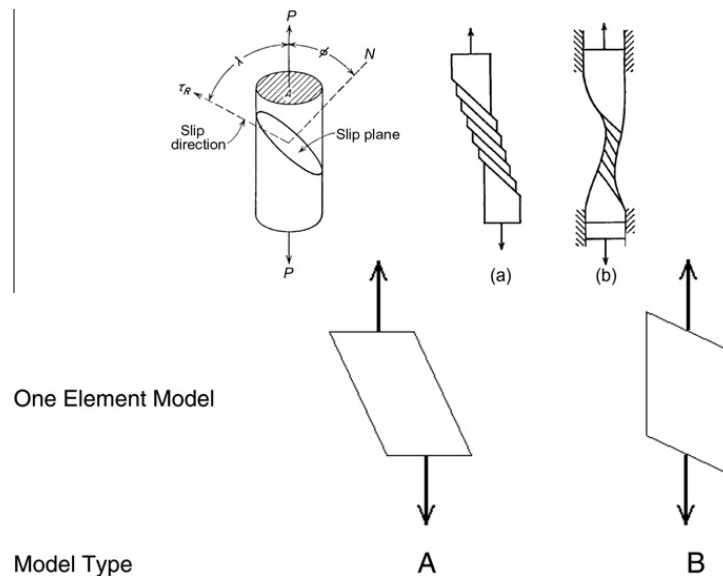


Fig. 5. Elements of disturbed lattice without constraint and with stiff constraint (from Dieter, 1988) and two types of boundary conditions applied to single elements to simulate simple tension.

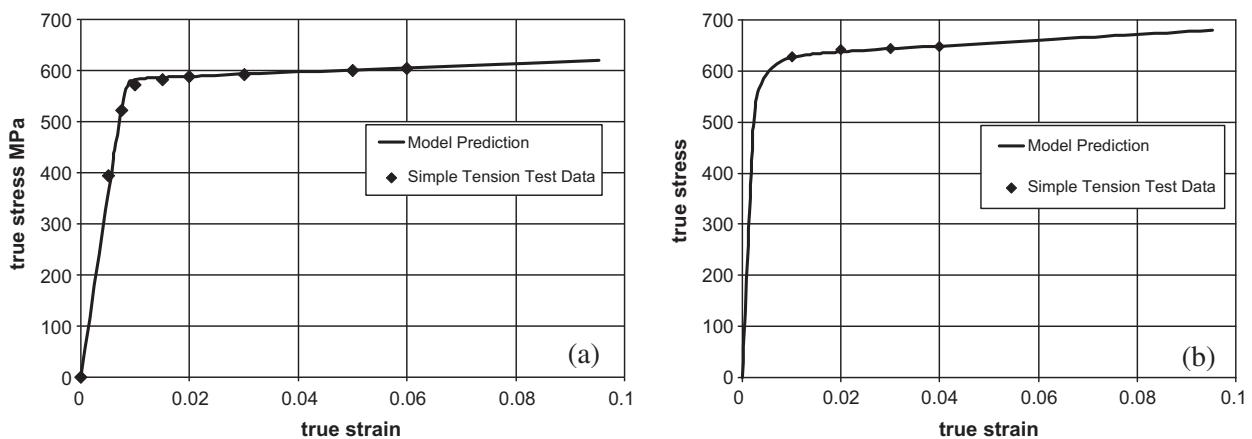


Fig. 6. Stress strain relations for simple tension along (a) $\langle 001 \rangle$ and (b) $\langle 111 \rangle$ crystallographic orientations at 982 °C.

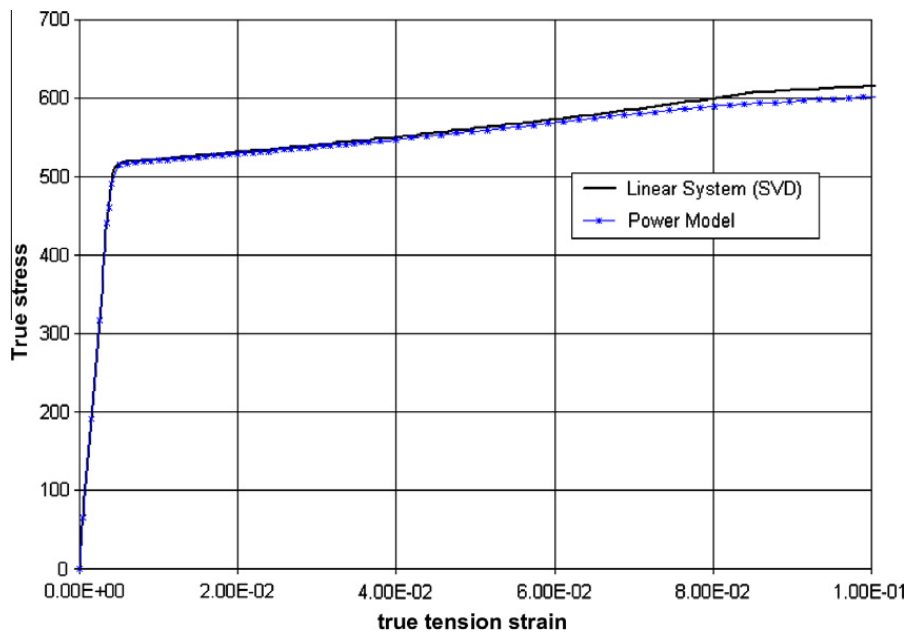


Fig. 7. Stress–strain relations for simple tension along $\langle 2\bar{3}6 \rangle$ crystallographic orientation obtained by rate-independent plasticity and by rate dependent power law with the value of the exponent equal to 80.

conducted simple tension simulations (type A) of a single crystal along $\langle 2\bar{3}6 \rangle$ crystallographic direction. The calculated stress–strain curves for 980 °C is shown in Fig. 7. The slip system activity is shown in Fig. 8. Deformation starts with a single octahedral slip system $(111)[\bar{1}01]$, then when the strain reaches about 8% the second conjugate slip system $(1\bar{1}\bar{1})[011]$ becomes active. It is important to note that the cube slip system $(001)[1\bar{1}0]$ is also active from the beginning, as can be seen from the plots in Fig. 8, but the total amount of cube slip system shear is much less than due to octahedral slip systems. The slip resistance of the conjugate slip system is larger than the slip resistance of the active one due to latent hardening. The effective resolved shear stress reaches the critical value at deformation levels slightly larger than for the non-hardening case² and subsequently the re-orientation slightly overshoots the stereographic triangle boundary $[001] - [\bar{1}11]$. After activation of the conjugate slip system $(1\bar{1}\bar{1})[011]$ the lattice rotates toward the $[\bar{1}11]$ pole along the triangle boundary. The prediction obtained by our rate-independent model is indistinguishably close to the predictions obtained by the power law (rate-dependent model) with the exponent value exceeding 80, which significantly increased the stiffness of the differential equations. It is important to note that the rate-dependent power law with small values of exponent specific for creep (3–5) predicts that more slip systems are active leading to more homogeneous deformation and slower crystal re-orientation. For example, for creep along $\langle 2\bar{3}6 \rangle$ crystallographic orientation slip systems $(111)[01\bar{1}]$ and $(1\bar{1}\bar{1})[\bar{1}0\bar{1}]$ are also active, however, total slip along these

systems is significantly smaller than along the primary and the conjugate ones.

Deformation along $\langle 2\bar{3}6 \rangle$ is very sensitive to the boundary conditions. The stress–strain relationship obtained under different types of boundary conditions, such as Type A as was reported above, type B loading, as well as numerical results from the cylinder specimen model are shown in Fig. 9. For type B loading conditions, deformation takes place along the single $(111)[\bar{1}01]$ slip system until collapse occurs by excessive deformation. Crystal re-orientation is rotated slightly toward the $[001]$ pole from the boundary conditions as shown in Fig. 10 together with prediction obtained for type A loading. We evaluated the one element prediction by comparing the numerical results against our 3744 element cylinder specimen model. The top and bottom of the numerical specimen are rigidly prevented from rotation and absolutely symmetric. In order to eliminate end-effects the last two layers of finite elements from each end are made elastic. We use 35 elastic–plastic central layers of finite elements and 96 elements in each cross-section as shown in Fig. 11. Deformation is very sensitive to any minor variation of boundary conditions and starts necking at deformation levels of about 7–10% as shown in Fig. 12. An increase in the number of elements does not change the character of deformation which appears to be very inhomogeneous. The central elements deform almost according to loading scheme A, while surface and near surface elements clearly deforms as type B elements. Due to inhomogeneities in the deformation the crystal lattice re-orientation of the central element is different than type A results but reasonably close to it as can be seen from Fig. 10. Due to the lack of the symmetry during the deformation the model predicts noticeable ovalization of the cross-section as shown in Fig. 13. Such an ovalization is specific for

² We performed modeling for the “theoretical” non-hardening case and the conjugate slip system became active exactly on the boundary of stereographic triangle.

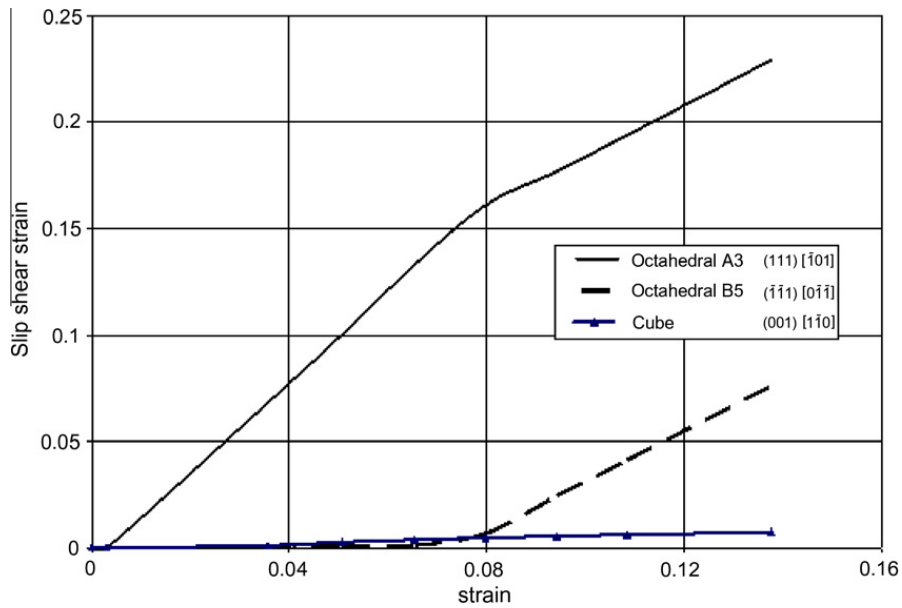


Fig. 8. Slip systems shear for simple tension of single crystal PWA 1484 along (236) crystallographic orientation.

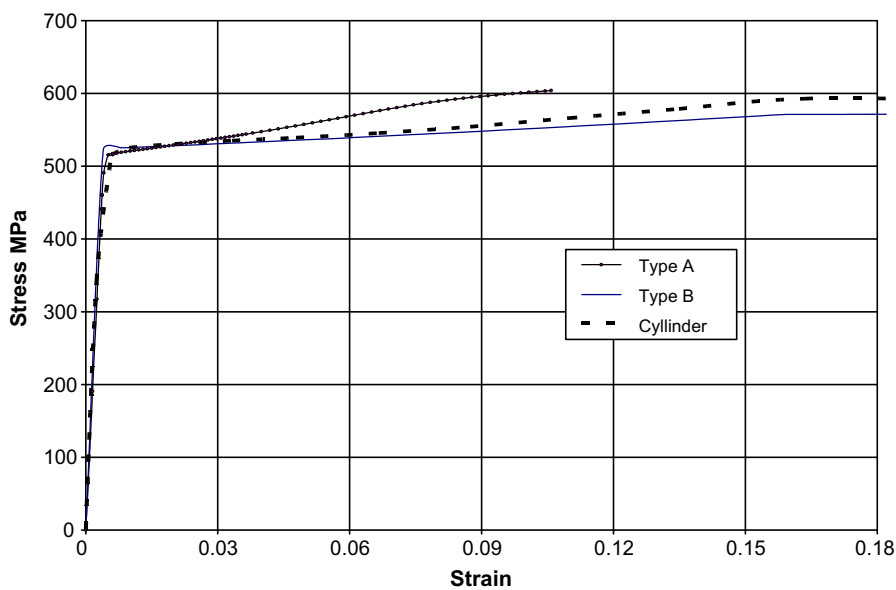


Fig. 9. Stress–strain relations for simple tension along (236) crystallographic numerically orientation obtained by applying different boundary conditions (single element type A and type B) and for an element in the 3744 – element cylinder model.

any non-corner crystallographic orientation and might be used for specimen life prediction as has been shown by Shah et al. (2004).

6.2. Model Implementation for cyclic loading

Most of the RI models were used to deal with monotonic loading response, but here we apply our approaches to cyclic loading schemes and verify our simulation predictions against test results obtained on PWA 1484 Ni-based superalloy at isothermal conditions. There are several well known observations that should be modeled while analyzing the cyclic tests:

- (i) Bauschinger effect – initial reduction of the reverse proportional limit and
- (ii) Cyclic softening – reduction of initially high hardening rate due to cyclic transient effects (Hu et al., 1992; Watanabe et al., 2002; Xu and Jiang, 2004).

The Bauschinger effect is controlled by the evolution equation for the back stress $\omega(t)$ (see Eq. (11)). During the reverse cycle the back stress is not yet steady and the absolute value of the effective stress $|\tau - \omega|$ reaches the critical value earlier than during the initial “forward” loading step. Experimental results (Lin, 1995) indicate that the cyclic softening effects are active only during transient

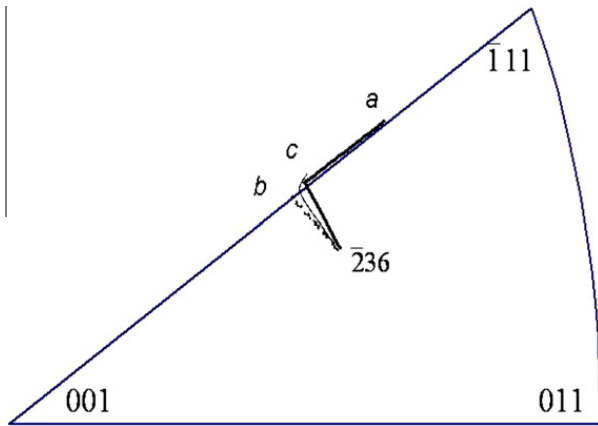


Fig. 10. Crystal lattice re-orientation of the single L1₂ crystal due to simple tension along $\langle 236 \rangle$ crystallographic axis; (a) type A boundary conditions, (b) type B loading conditions, and (c) central element of the cylinder model.

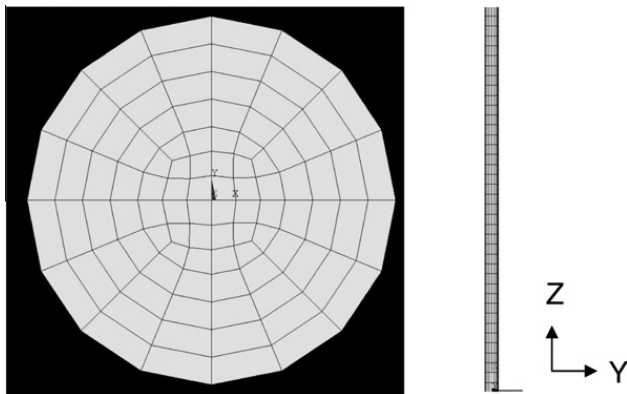


Fig. 11. Cylinder FEM used for the simulation of single crystal tensile sample.

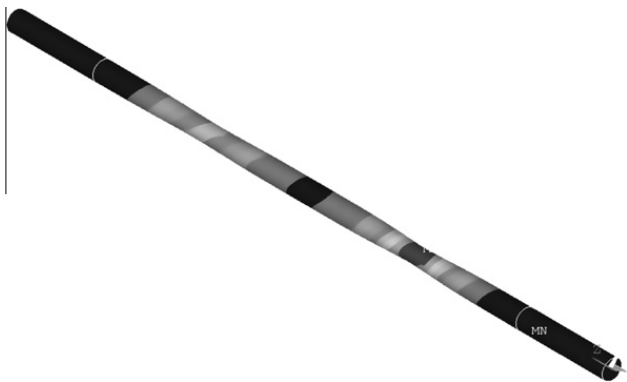


Fig. 12. Stereographic view of the necked $\langle 236 \rangle$ single crystal specimen after overall tension to 20%.

regime which is approximately equal to the time needed for the back stress to change sign, therefore, they will be important if dwell effects (creep-fatigue interaction) are considered. During creep-fatigue interaction the dislocation cells structure is dissolving while the back stress and the effective RSS have different signs and the dislocation growth rate slows down. We simulate this effect by cor-

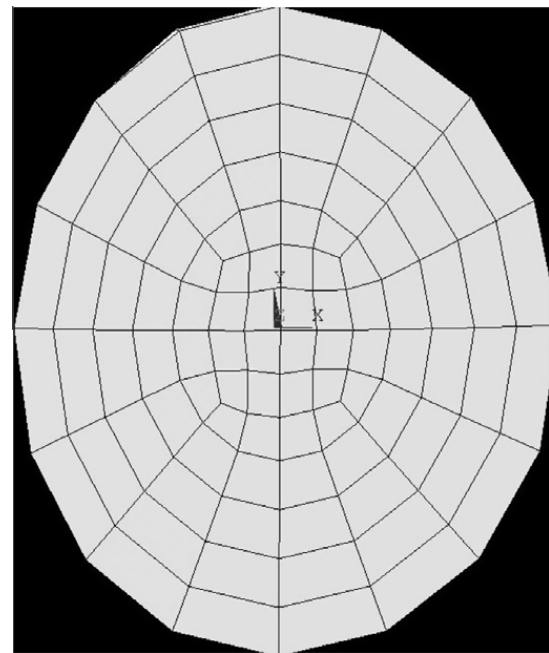


Fig. 13. Elliptical cross-section in the necked part of the specimen.

recting a mobile dislocation rate term in Eq. (12) with a cyclic softening term proportional to $\text{sign}(\dot{\omega}^\alpha \cdot \dot{\gamma}^\alpha)$:

$$\zeta^\alpha = \frac{1}{2} \{ 2 - \eta [1 - \text{sign}(\dot{\omega}^\alpha \cdot \dot{\gamma}^\alpha)] \} \quad (19)$$

where the parameter η has to be adjusted to reflect the intensity of cyclic softening. In our calculations, we used $\eta = 1$, which means that there is a non-hardening plateau during transient unloading. The signum function in Eq. (19) is used to produce a step change in ζ^α when the sign of $\dot{\omega}^\alpha \cdot \dot{\gamma}^\alpha$ changes. Evolution equations for mobile dislocations along each slip system are modified in the following way:

$$\dot{\rho}_m^\alpha = \zeta^\alpha M \left(\frac{\tau^\alpha - \omega^\alpha}{s^\alpha} \right) \dot{\gamma}^\alpha \left(\frac{\varepsilon^2 \rho_m^{ss} + \rho_p^{ss} - \rho_p^\alpha - \varepsilon^2 \rho_m^\alpha}{\rho_0} \right) \quad (20)$$

If the back stress and the effective RSS have the same signs the dislocation microstructure deforms in similar to monotonic loading with the parameter $\zeta \equiv 1$.

Otherwise, if the signs of the back stress and slip shear rate are opposite, the dislocation cells structure is dissolving and the dislocation growth rate slows down. It is important to note that during any monotonic loading parameter $\zeta \equiv 1$ and Eq. (20) is identical to (12).

During reasonably fast strain-controlled LCF tests, our results have demonstrated this effect is small.

Results of the model implementation against test data are shown in Figs. 14–16. Fig. 14(a–c) shows a comparison of model prediction against experimental data for $\langle 001 \rangle$ single crystal PWA 1484 cyclically loaded up to a 1% strain amplitude at a temperature of 870 °C. Due to strain hardening the overall loops shift up in the stress–strain plane and the hysteretic loop is getting narrower. We present the modeling results together with measured test data for the first cycle (Fig. 14a) and cycle

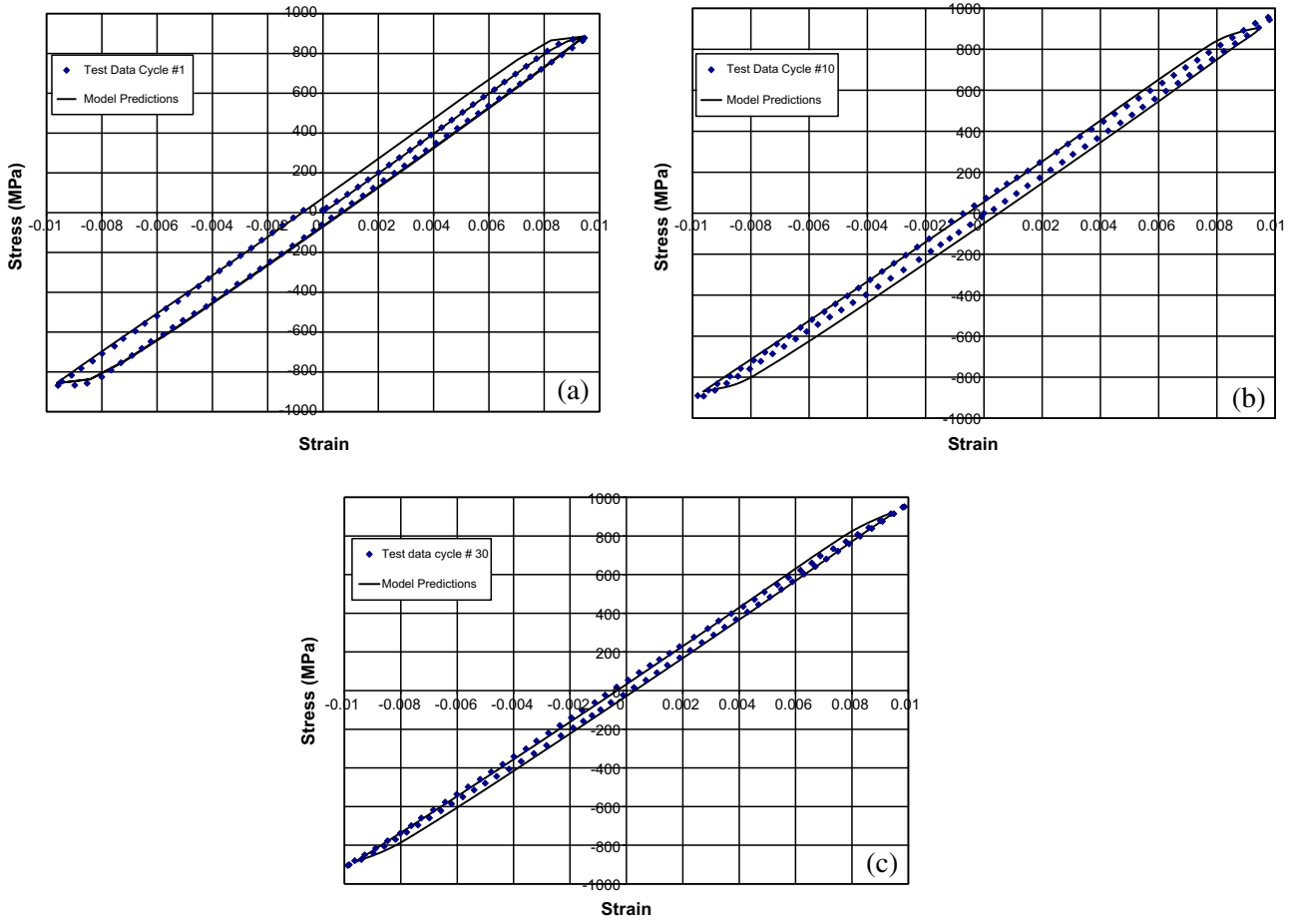


Fig. 14. Predicted stress–strain relations against experimental data for strain-controlled cyclic test up to 1% strain along $\langle 001 \rangle$ crystallographic direction at 870 °C. Results are shown for the first cycle (a), cycle 10 (b), and cycle 30 (c).

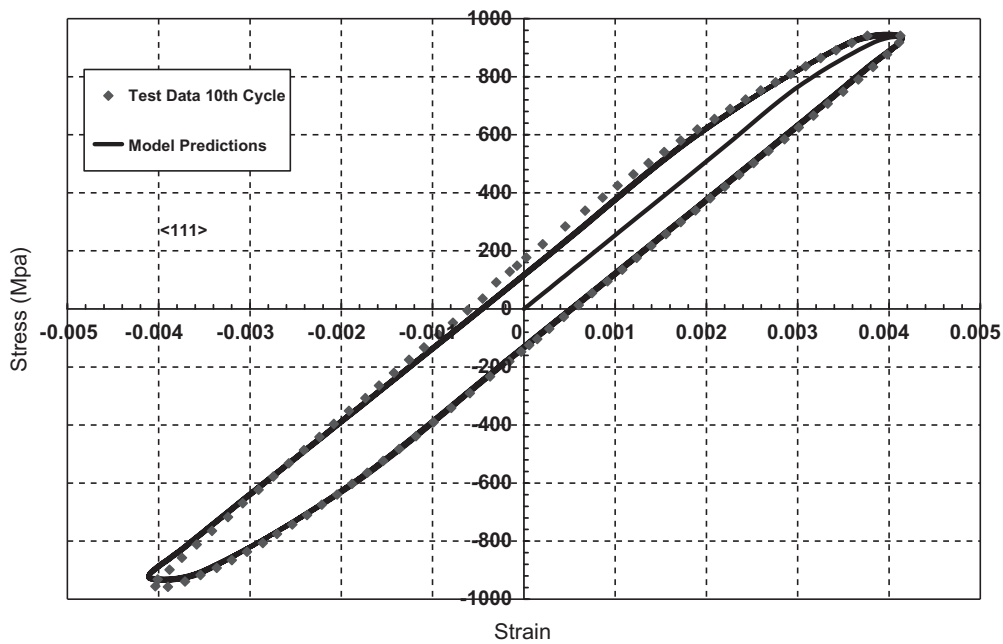


Fig. 15. Predicted stress–strain relations against experimental data for strain-controlled cyclic test up to 0.8% strain range along $\langle 111 \rangle$ crystallographic direction at 870 °C.

#10 (Fig. 14b), as well as cycle #30 (Fig. 14c) where the cyclic loop is stabilized. One can see that simulation results are extremely close to the test observations. Fig. 15 shows stress–strain relations for $\langle 111 \rangle$ oriented single crystal cyclically deformed under strain-controlled conditions to the mechanical strain range of 0.8% at temperature of 870 °C. Due to the high Young's modulus the yield is more pronounced along the $\langle 111 \rangle$ orientation

and the loop is wider open than at the similar loading conditions along the $\langle 001 \rangle$ crystallographic direction. Comparison of predicted vs. measured data demonstrates the high quality predictions of the model. Modeling results obtained for $\bar{1}23$ single slip orientation compared against test data are shown in Fig. 16 for the isothermal conditions of 870 °C and strain range of 0.8% with $R = -1$. The deformation starts with $(111)[01\bar{1}]$ single slip system.

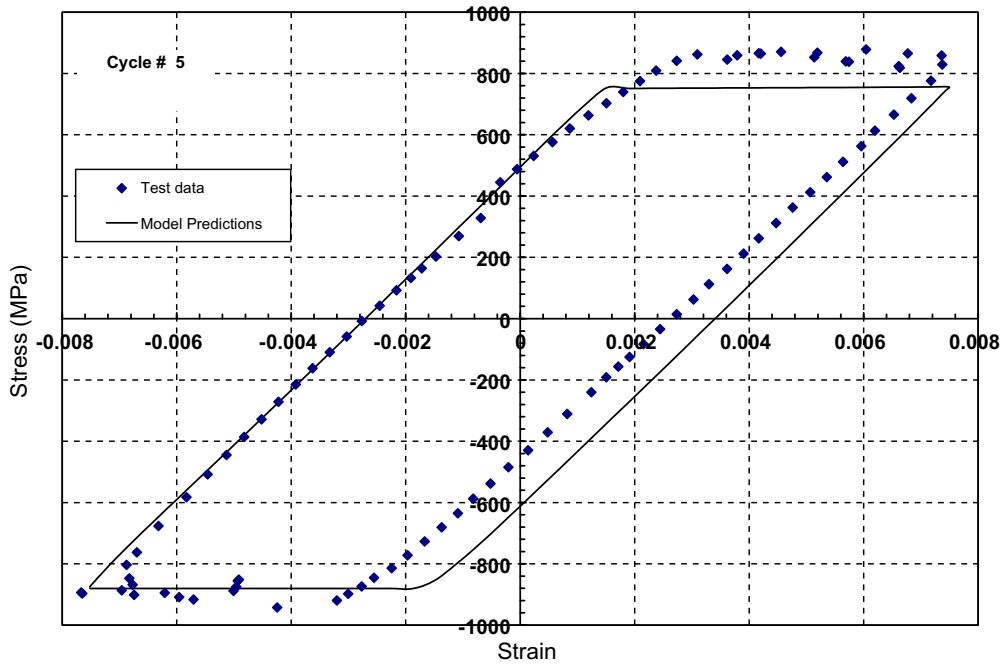


Fig. 16. Predicted stress–strain relations against experimental data for strain-controlled cyclic test up to 0.8% strain range along $\bar{1}23$ crystallographic direction at 870 °C.

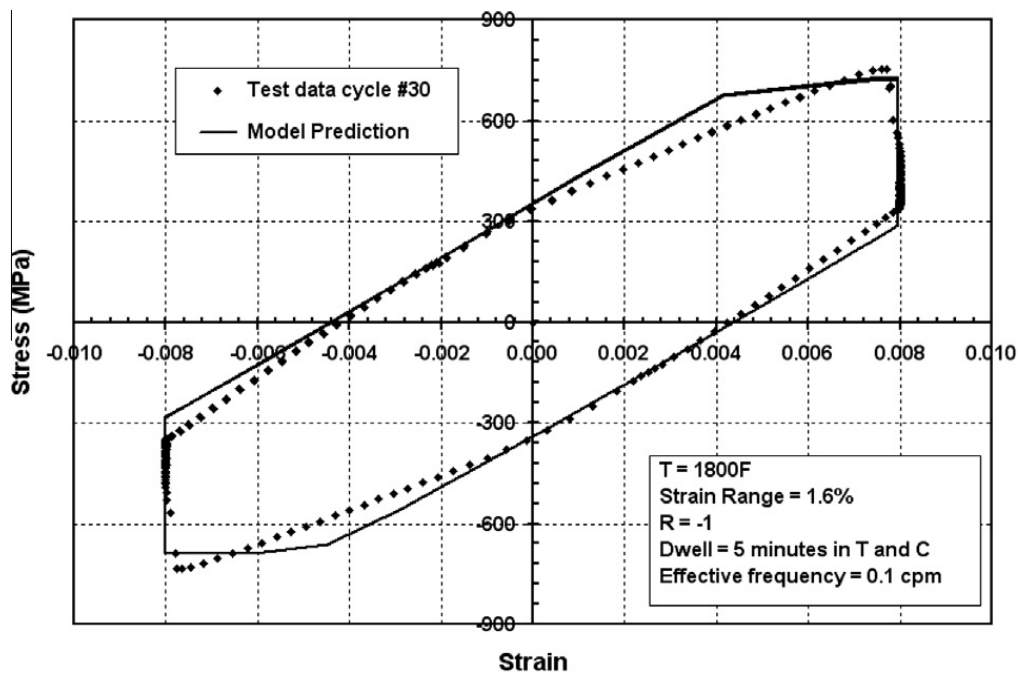


Fig. 17. Test data and model predictions of creep-fatigue interaction with 5 min dwell time at tension and compression for strain-controlled cyclic test up to 0.8% strain range along $\langle 001 \rangle$ crystallographic direction at 982 °C. Stress–strain loops stabilize by cycle #30.

The loop is extremely wide due to the relatively low yield value for the single crystal along single slip crystallographic direction. Errors of the numerical prediction are less than 10% which is good for a single slip crystallographic orientation. Model predictions can be improved by refining with tension–compression asymmetry properties in the model. We did not pay attention to this issue in this work. Finally, we conduct the creep–fatigue interaction test at 982 °C to the mechanical strain amplitude of 0.8%. We hold a constant strain for 5 min at both tension (*T*) and compression (*C*) maximum strain conditions (generating stress relaxation) during each cycle. The stress–strain curves calculated and measured at the cycle #30 are shown in Fig. 17. The numerical correction (19) and (20) appear to be important for model prediction of ratcheting during stress–strain loop stabilization.

The numerical results demonstrate that our combined creep–rate-independent elastic–plastic model is capable of obtaining extremely good predictions for both the monotonic and the cyclic elastic–plastic–viscoplastic response of a $L1_2$ single crystal.

7. Concluding remarks

We have developed a comprehensive combined creep–RI plasticity constitutive model and have implemented it in the commercial finite element software ANSYS as a material user routine. The equations governing the mechanical response have been calibrated using existing creep and simple tension elastic–plastic experimental data. The model predicts the crystallographic lattice rotation during deformation, which is important during material processing and cyclic ratcheting, especially around geometrical features such as cooling holes in single crystal turbine blades. The model also predicts material yield anisotropy and yield – thermal dependence.

Our combined creep and rate-independent cyclic crystal plasticity formulation accurately describes monotonic as well as cyclic loading for a wide range of generic non-isothermal conditions. The model can uniquely determine the amount of shear along active slip systems at each increment and predicts cyclic ratcheting, loop stabilization and cyclic softening due to dwell time. The developed approach is numerically robust and efficient, allowing numerical analysis of tens and even hundreds cycles providing a working tool for low cycle fatigue (LCF) and thermal mechanical fatigue (TMF) prediction analyses. Based on our modeling results and their comparison with experiments it is possible to conclude the following:

- (1) Our rate-independent plasticity model does not interfere with time dependent creep effects and provides reliable results over a wide range of loading conditions from fast LCF test to long creep and creep–fatigue regimes.
- (2) A physics-based crystal plasticity model combining latent and kinematic hardening, dislocation density evolution under monotonic and cyclic loading has been developed and verified against monotonic and cyclic set of tests.

- (3) The combined creep–RI plasticity model has been extended to cyclic loading conditions. Our model, calibrated against monotonic tensile creep and elastic–plastic responses, accurately predicts cyclic behavior with and without stress relaxation (dwell time).
- (4) The major deformation mechanisms of high temperature creep and plasticity of Ni-based single crystal superalloy are octahedral $\{111\}(110)$ and cube $\{001\}(110)$ crystallographic slip.
- (5) Single slip crystallographic orientations deform mostly non-homogeneously, which leads to necking and subsequently shorter life.
- (6) Ovalization of the plastically deformed single crystal specimen can be readily predicted and might be correlated with time to failure.

The combined theoretical–numerical–experimental study of single crystal PWA 1484 Ni-based superalloy reported here increases our understanding of viscoplastic deformation in $L1_2$ systems; it holds substantial promise through future work and through further refinement. In particular, the model can be used to more accurately account for the thermal–cyclic effects and for non-homogeneous transient temperature effects on a deformation.

Acknowledgements

The authors are grateful for support and funding from the United States Air Force Research Laboratory through contract #FA8650-07-C-5252 and to Dr. Andrew Rosenberger for his support and attention to this work. Authors also would like to thank Prof. Alan Needleman for fruitful discussions and Dr. V. Seetharaman for his help with experimental program.

References

- Allan, C., 1995. Plasticity of Nickel Base Single Crystal Superalloys. Ph.D. Thesis, MIT.
- Anand, L., Kothari, M., 1996. A computational procedure for rate-independent crystal plasticity. *J. Mech. Phys. Solids* 44, 525–558.
- Asaro, R.J., 1983. Crystal Plasticity. *ASME J. Appl. Mech.* 50, 921–934.
- Asaro, R.J., Needleman, A., 1985. Texture development and strain hardening in rate-dependent polycrystals. *Acta Metall.* 33, 923–953.
- Chaboche, J.L., 1986. Time-independent constitutive theories for cyclic plasticity. *Int. J. Plasticity* 2, 149–188.
- Dieter, G.E., 1988. *Mechanical Metallurgy*. McGraw-Hill Co, London.
- Hu, Z., Rauch, E.F., Teodosiu, C., 1992. Work hardening behavior of mild steel under stress reversal at large strains. *Int. J. Plasticity* 8, 839–856.
- Kachanov, L.M., 1986. *Introduction to the Theory of Damage*. Martinus Nijhoff, Hague.
- Kalidindi, S.R., Anand, L., 1994. Macroscopic shape change and evolution of crystallographic in pre-textured f.c.c. metals. *J. Mech. Phys. Solids* 42, 459–490.
- Kalidindi, S.R., Bronkhorst, C.A., Anand, L., 1992. Crystallographic texture evolution during bulk deformation processing of f.c.c. metals. *J. Mech. Phys. Solids* 40, 537–569.
- Krempf, E., Wells, C.H., Zudans, Z., 1976. Workshop on Inelastic Constitutive Equations for Metals: Experimentation–Computation–Representation. Rensselaer Polytechnic Institute, Troy, New York.
- Lemaitre, J., 1996. *A Course on Damage Mechanics*. Springer, Berlin, 228 p.
- Lin, C.C., 1995. Cyclic deformation of FCC crystals. MS Thesis, MIT.
- Nissley, D., Meyer, T., Walker, K., 1991. Life Predictions and Constitutive Models for Engine Hot Section Anisotropic Materials, Pratt & Whitney. Report NAS3-23939.
- Orowan, E., 1940. Problems of plastic gliding. *Proc. Phys. Soc.* 52, 8–22.

- Shah, D.M., Vega, S., Woodard, S., Cetel, A.D., 2004. Primary creep in nickel-base superalloys in superalloys 2004. In: Green, K.A., Pollock, T.M., Harada, H., Howson, T.E., Reed, R.C., Schirra, J.J., Walston, S. (Eds.), TMS, pp. 197–206.
- Staroselsky, A., Anand, L., 1998. Inelastic deformation of polycrystalline face centered cubic materials by slip and twinning. *J. Mech. Phys. Solids* 46 (4), 671–696.
- Staroselsky, A., Cassenti, B., 2008. Mechanisms for tertiary creep of single crystal superalloy. *Mech. Time-Depend. Mater.* 12, 275–289.
- Stouffer, D.C., Dame, L.T., 1996. *Inelastic Deformation of Metals*. John Wiley & Sons, Inc.
- Voyiadjis, G.Z., Huang, W., 1996. A modeling of single crystal plasticity with back-stress evolution. *Eur. J. Mech. A* 319–321, 63–73.
- Walker, K.P., 1980. Representation of Hastelloy-X Behavior at Elevated Temperature with a Functional Theory of Viscoplasticity. Presented at ASME/PVP Century 2 Emerging Technology Conference. San Francisco, California.
- Watanabe, C., Kanmuri, K., Kato, M., Onaka, S., Fuji, T., 2002. Rearrangement of fatigue dislocation structure in copper single crystals associated with reduction in the plastic strain amplitude. *Phil. Mag. A* 82, 1317–1330.
- Weng, G., 1979. Kinematic hardening rule in single crystals. *Int. J. Solids Struct.* 15, 861–870.
- Weng, G., 1980a. Dislocation theories of work hardening and yield surfaces of single crystals. *Acta Mechanica* 37, 217–230.
- Weng, G., 1980b. Constitutive equations of single crystals and polycrystalline aggregates under cyclic loading. *Int. J. Eng. Sci.* 18, 1385–1397.
- Xu, B., Jiang, Y., 2004. A cyclic plasticity model for single crystal. *Int. J. Plasticity* 20, 2161–2178.